

White-light superflare and long-term activity of the nearby M7 type binary EI Cnc observed with GWAC system

HUA-LI LI,¹ JING WANG,^{2,1} LI-PING XIN,¹ JIAN-YING BAI,¹ XU-HUI HAN,¹ HONG-BO CAI,¹ LEI HUANG,¹ XIAO-MENG LU,¹ YU-LEI QIU,¹ CHAO WU,¹ GUANG-WEI LI,¹ JING-SONG DENG,^{1,3} DA-WEI XU,^{1,3} YUAN-GUI YANG,⁴ XIANG-GAO WANG,² EN-WEI LIANG,² AND JIAN-YAN WEI¹

¹CAS Key Laboratory of Space Astronomy and Technology, National Astronomical Observatories, Chinese Academy of Sciences, Beijing 100101, China.

²Guangxi Key Laboratory for Relativistic Astrophysics, School of Physical Science and Technology, Guangxi University, Nanning 530004, China

³School of Astronomy and Space Science, University of Chinese Academy of Sciences, Beijing, China

⁴School of Physics and Electronic Information, Huaibei Normal University, Huaibei 235000, China.

(Received 2023 May 23; Accepted 2023 July 6)

Submitted to ApJ

ABSTRACT

Stellar white-light flares are believed to play an essential role on the physical and chemical properties of the atmosphere of the surrounding exoplanets. Here we report an optical monitoring campaign on the nearby flaring system EI Cnc carried out by the Ground-based Wide Angle Cameras (GWAC) and its dedicated follow-up telescope. A superflare, coming from the brighter component EI CncA, was detected and observed, in which four components are required to properly model the complex decay light curve. The lower limit of flare energy in the R -band is estimated to be 3.3×10^{32} ergs. 27 flares are additionally detected from the GWAC archive data with a total duration of 290 hours. The inferred cumulative flare frequency distribution follows a quite shallow power-law function with a slope of $\beta = -0.50 \pm 0.03$ over the energy range between 10^{30} and 10^{33} erg, which reinforces the trend that stars cooler than M4 show enhanced superflare activity. The flares identified in EI Cnc enable us to extend the $\tau - E$ relationship previously established in the white-light superflares of solar-type stars down to an energy as low as $\sim 10^{30}$ erg (i.e., by three orders): $\tau \propto E^{0.42 \pm 0.02}$, which suggests a common flare mechanism for stars with a type from M to solar-like, and implies an invariant of $B^{1/3}v_A$ in the white-light flares.

Keywords: flare — stars: individual (EI Cnc)—techniques: photometric— techniques:

1. INTRODUCTION

M dwarfs occupy a majority ($\sim 70 - 75\%$) of the local stellar population (Chabrier & Baraffe 1997; Henry et al. 2006; Bochanski et al. 2010).

Corresponding author: Huali Li, Jing Wang
lhl@nao.cas.cn, wj@nao.cas.cn

A large fraction of M dwarfs are magnetically active with flares more energetic than those of the Sun (Hawley et al. 2014). Compare to solar-like and early-M stars, the understanding of the dynamo pattern is a challenge for the ultra-cool dwarfs (UCDs) (Chabrier & Baraffe 1997; Mohanty et al. 2002), because the solar-type shell dynamo is hard to be supported in UCDs due to the lack of the tachocline - a narrow boundary layer separating the convective and radiative zones (Mohanty et al. 2002; Charbonneau 2014; Kochukhov 2021).

Flares from UCDs have been ubiquitously observed in multi-wavelength, including near-infrared (Kanodia et al. 2022), optical bands (e.g., Fuhrmeister & Schmitt 2004; Stelzer et al. 2006; Schmidt et al. 2014, 2016; Gizis et al. 2017; Paudel et al. 2018; Xin et al. 2021, 2023), ultraviolet, and X-ray (e.g., Fleming et al. 2000; Stelzer et al. 2006; Robrade et al. 2010; De Luca et al. 2020). Gizis et al. (2000) estimated a flaring frequency of 7% or higher during the whole life of the late-type stars with the studies of a sample of 53 nearby M7-M9.5 dwarfs, suggesting that flaring is common among ultracool dwarfs. In addition, Hawley et al. (2014) estimated that the flaring time of active and inactive stars varies between $\sim 30\%$ and $\sim 0.01\%$ at a level detectable with *Kepler*. Paudel et al. (2018) reported a total of 283 flares from 10 UCDs by using the *Kepler* K2 short-cadence data. With a sample of 1392 flare events, Medina et al. (2020) found a high value of flaring frequency of 26% from 125 single mid- to late-M dwarfs, in which 60% of the sample had flared one or more times. In addition, Murray et al. (2022) have recently identified 234 flares from 85 flaring UCDs by the SPECULOOS-South survey program, suggesting that M5-M7 stars are more likely to flare than both earlier and later M dwarfs. The flares of UCD is crucial to understand not only how the magnetic energy

is converted to gas kinetic energy within the thick convective atmospheres (e.g., Barnes 2003; Morin et al. 2010; McLean et al. 2012), but also the relation between the activities of stars and the habitability of an exoplanet. Due to their close proximity of habitable zone, the close-in planetary companions are more likely to be exposed to the high-energy radiation and particles from the hosts (e.g., Khodachenko et al. 2007; Lammer et al. 2007; Shields et al. 2016). On the one hand, it is suggested that the ultraviolet radiation and ionized particles released in flares may initiate chemistry relevant to the origin of life (Ranjan et al. 2017; Rimmer et al. 2018). On the other hand, it may have effects on the chemical compositions of planetary atmospheres (e.g., Lammer et al. 2007; Segura et al. 2010; Tilley et al. 2019). Theoretical studies suggest that no significant ozone layer destruction occurs, if the flares output mainly consists of photons rather than energetic particles (e.g., Segura et al. 2010; Tilley et al. 2019; Zeldes et al. 2021; Murray et al. 2022).

Here we report an optical monitoring campaign of red dwarf EI Cnc carried out by the ground-based wide angle cameras (GWAC), a ground facility of the SVOM mission (Space-based multi-band astronomical Variable Objects Monitor, Wei et al. (2016)). With a white-light superflare captured by the GWAC in real-time, rapid multi-wavelength follow-ups were carried out by a narrow-field optical telescope. In addition, 27 more flares were identified in the GWAC's archived data.

The paper is organized as follows. The properties of EI Cnc and the used instruments procedure are described in Section 2. Section 3 presents the superflare and the light curve analysis. The off-line search of the flares of the object in GWAC archive data is shown in Section 4. Section 5 presents the resulted cumulative flare energy distribution. A discussion is given in Section 6.

2. THE OBJECT AND OBSERVATION

2.1. *EI Cnc*

EI Cnc (G9-38AB, GJ1116AB) is a nearby red dwarf system whose flaring activity was first reported by [Pettersen & Evans \(1985\)](#). This source is located at a distance of about 5.13 pc (5.136 ± 0.003 , 5.126 ± 0.005 , [Gaia Collaboration et al. \(2018\)](#)), consisting of two nearly identical dwarfs with spectral type of M7+M7 ([Newton et al. 2014](#)). EI CncA corresponds to the brighter component with $M_V \sim 15.46$ mag and EI CncB the fainter one with $M_V \sim 16.31$ mag ([Reid & Gizis 1997](#)). The basic properties of both components are listed in [Table 1](#). The two components were reported to be separated by 1.39 ± 0.01 arcsec ([Law et al. 2008](#)). Recent measurement given in Gaia DR2 returns a consistent value of 1.37 ± 0.01 arcsec at the epoch of 2015.9 ([Gaia Collaboration et al. 2018](#)). By adopting a circular orbit and a total mass of $0.2M_\odot$, the projected separation and orbital period are estimated to be 7.0 AU and at least 42 years, respectively.

[Pettersen \(1985\)](#) detected 24 flares in *U*-band from this object within 4.5 hours. The *U*-band energy released in the flares ranges from 10^{28} to $10^{30.5}$ erg. The object is listed in the nearby flare star catalog compiled by [Pettersen \(1991\)](#), and is considered to be slightly less active than the close binary FL Vir (Wolf 424) ([Pettersen 2006](#)). EI Cnc is known as a relatively strong X-ray source with $\log L_X/\text{erg s}^{-1} = 27.5 - 27.6$ in the ROSAT/PSPC catalog ([Schmitt et al. 1995](#); [Fleming et al. 1995](#); [Schmitt & Liefke 2004](#)). A major X-ray flare with a detection of Fe XIII coronal line was reported by [Fuhrmeister et al. \(2004\)](#).

2.2. *The observational facility*

The Ground-based Wide Angle Cameras (GWAC), located at Xinglong observatory of National Astronomical Observatories, Chinese Academy of Sciences, is an array of telescopes

with wide-angle cameras dedicated to optical transient survey ([Wei et al. 2016](#)). It monitors the sky with the cadence of 15 seconds (i.e., 10 seconds for exposure and 5 seconds for readout), aiming to detect short-duration transients such as gamma-ray bursts ([Xin et al. 2023](#)), stellar flares ([Wang et al. 2021, 2022](#); [Li et al. 2023](#)), optical counterpart of gravitational waves ([Turpin et al. 2020](#)) and fast radio bursts ([Xin et al. 2021](#)). Currently, the GWAC is composed of four units. Each unit is composed of four identical cameras (JFoV) each with an aperture of 18cm, and one camera (FFoV) with an aperture of 3.5cm that is used to capture the bright transients that are saturated in the JFOV. The limiting magnitudes of JFoV and FFOV is typical of 16 and 12 magnitude in the *R*-band, respectively. The total field-of-view of the current GWAC is about 2200 square degree. More details of the GWAC are provided in [Wang et al. \(2020\)](#) and [Han et al. \(2021\)](#).

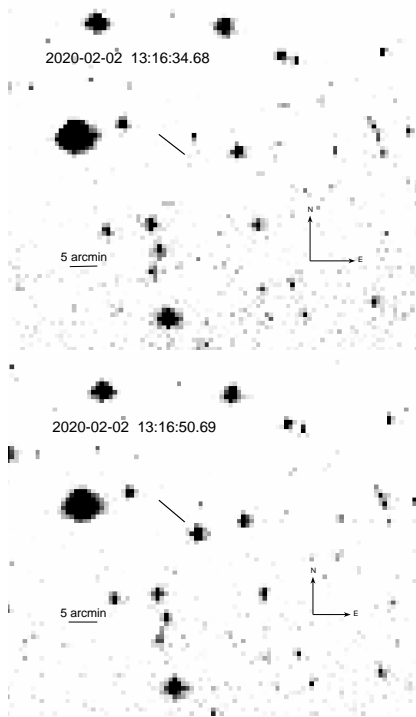
3. THE SUPERFLARE ON 2020-02-02

3.1. *The observations*

On 13:16:50 UT Feb. 2, 2020, a white light flare of EI Cnc was captured in real-time by an FFOV camera during its normal survey. [Figure.1](#) displays the reference image (upper panel) and discovery image (lower panel). The object was continuously observed by the GWAC from UT12:59:19.6 to 13:31:14.7, lasting for about half an hour in the field of FFOV on the night. During the observation, the limiting magnitude of FFOV in the *R*-band is determined to be about 11.8 ± 0.2 mag for each single exposure. The flare decays rapidly to the detection limit of the FFOV at 2.5 minutes after the trigger. Since the observations were continuous with a cadence of 15 seconds, the first brightest measurement is believed to be near the real peak within the temporal resolution, which means the bright-

Table 1. Properties of EI Cnc extracted from various surveys.

Parameter	EI CncA	EI CncB
M_V (mag)	15.46	16.31
Position in Gaia DR2 ¹		
R.A.(2015.5)	134.5593 ± 0.09522	134.55883 ± 0.13486
Decl.(2015.5)	19.76297 ± 0.06141	19.76258 ± 0.08959
Parallax (mas)	194.7225 ± 0.12507	195.08365 ± 0.17542
Spectral classification		
Spectral type	M7	M7
T_{eff} (K)	2905 ± 105 ²
Proper motion ¹		
μ_α (mas yr ⁻¹)	-766.02903 ± 0.19043	-938.54588 ± 0.25592
μ_δ (mas yr ⁻¹)	-99.26976 ± 0.12183	-36.23736 ± 0.17225

¹Gaia Collaboration et al. (2021)²Wang et al. (2022)**Figure 1.** Images of the superflare of EI Cnc obtained by the GWAC FFoV on 2020-02-02. The upper panel is the reference image which was obtained about 15 sec before the triggered of the flare (the lower panel). The observation times, direction and spatial scale are labeled in both images.

ness was brightened by more than 2.3 magnitudes in 15 seconds during its rising phase¹.

A robotic follow-up observation in standard Johnson-Cousins R -band was then carried out by the F60A telescope² located beside the GWAC cameras via the dedicated real-time automatic transient validation system (RAVS, Xu et al. (2020)). The follow-up observation started on UTC 13:18:23.5, i.e., 102 seconds after the trigger time of the flare, and lasted for 5.5 hours in total.

3.2. Data process

The images taken by both GWAC FFoV and F60A telescope were processed by the standard procedure, including bias, dark, and flat-field corrections, using the IRAF³ package. In the

¹ Such brightening results in a saturation in the JFOV images.

² The telescope with a diameter of 60cm has a f -ratio of 8.0, and is equipped with an Andor 2k \times 2k CCD. The corresponding pixel scale is 0.52 arcseconds per pixel.

³ IRAF is distributed by the National Optical Astronomical Observatories, which are operated by the Association of Universities for Research in Astronomy, Inc., under cooperative agreement with the National Science Foundation.

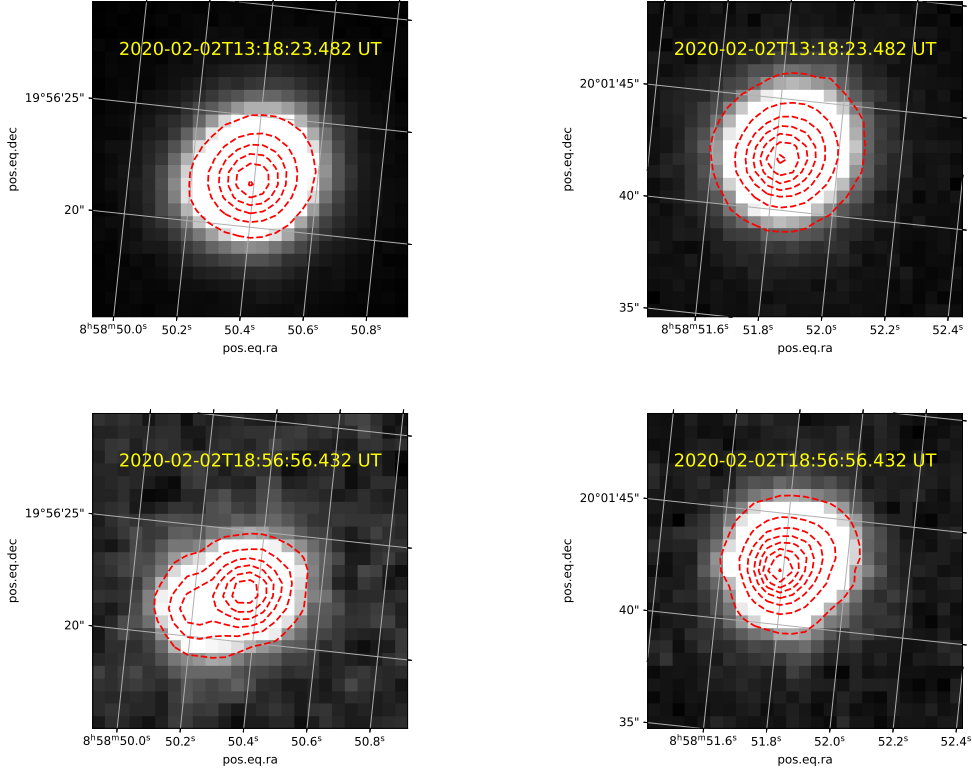


Figure 2. The 25×25 pixels R -band images of the field of EI Cnc obtained by the F60A telescope in 2020-02-02 (the original size of the image is 19.5×19.5 arcmin²). The left and right columns correspond to the object and the comparison star, respectively. The upper row shows the first image obtained at 2020-02-02UT13:18:23.482, while the bottom rows the last image at UT18:57:20.759, about 5.5 hours later than the first one.

subsequent aperture photometry, the aperture was adopted to be 3.0 and 10.0 pixels for the images taken by the FFoV and F60A, respectively. In order to combine the light curves resulted from FFoV and F60A, we used a relatively large aperture for the F60A images to enclose both components of the object, both because the two components are marginally resolved in the F60A images even at the quiescent state and because of the low spatial resolution of the FFoV images. Absolute photometric calibration was performed using the USNO B1.0 catalogue (Monet et al. 2003). The comparison stars used in our differential photometry are tabulated in Table 2.

3.3. Determine the source of the superflare

Table 2. The comparison stars used to calibrate the light curve of EI Cnc. The $R2$ and $B2$ magnitudes are derived from the USNO B1.0 catalog (Monet et al. 2003).

GWAC camera or telescope	R.A. (J2000)	Decl. (J2000)	$R2$ mag	$B2$ mag
GWAC/FFoV	134.715109	19.800973	9.19	9.89
F60A	134.564123	19.851556	11.62	11.09

Figure.2 shows the brightness contour of the R -band images obtained by F60A at two epochs. According to our astrometry, the contour was centered at EI CncA near the peak of the flare. While, the contour shape was lengthened by the contribution of EI CncB as the flare faded out, although the brightness was still

dominated by EI CncA. This analysis enables us to claim that the superflare occurring in 2020-02-02 is produced by the brighter component EI CncA, thanks for the rapid follow-ups by F60A with relatively higher spatial resolution of 0.52 arcseconds per pixel.

3.4. Properties of the light curve

Figure.3 shows the temporal variation of the calculated fractional flux in the R -band of the superflare. The fractional flux is calculated by adopting a quiescent specific flux of $F_{R,q} = 1.24 \times 10^{-14} \text{ erg cm}^{-2} \text{ s}^{-1} \text{ \AA}^{-1}$ that is transformed from the quiescent brightness of $R = 12.87 \text{ mag}$ extracted from the USNO B1.0 catalogue.

Although the sky field where the EI Cnc locates in has been monitored by FFoV long enough before the flare occurred, the rising phase of the superflare was not recorded, which suggests a quite fast rising with a rate of $> 0.16 \text{ mag s}^{-1}$, if the corresponding limit magnitude is used a reference. By adopting quiescent brightness is adopted as a reference, the rising rate is expected to be less than 0.24 mag s^{-1} .

With the high cadence of 15 seconds, we are able to study the decay behavior of the superflare in more details by modeling the decay phase with the following formula:

$$\frac{F_{\text{decay}}}{F_{\text{amp}}} = \sum_{i=1}^n a_i e^{-k_i \times t/t_{1/2}} \quad (1)$$

where F_{amp} is the peak flux of the light curve, a the amplitude of the component, k the decay index for each component, and t the time after the trigger time. $t_{1/2}$ is the decay duration from the peak to the half of the peak. The Bayesian information criterion (BIC) is adopted in the modeling to test whether the fitting is overfitted or not. The BIC value is 137.33 for the model with 3 components, while 75.46 for the model with 4 components. The result indicates that the 4-component model is the best one with a reduced $\chi^2/\text{d.o.f.} = 13.10$ and a de-

gree of freedom of 47. The best fit model is shown in Fig.3 by different colors. The values of the corresponding parameters are tabulated in the Table 3.

During the modeling of the superflare, only the peak time to 2500 seconds of the light curve was analysed. The brightness after 2500 seconds was not integrated since the later light curve had become too shallow which was likely not part of the flare, but might be caused by the variation of the object itself.

Given the best fit model, the equivalent duration time (ED), the time needed to emit the flare energy at the quiescent level, is estimated to be 5293 seconds or ~ 1.5 hours. With the distance of 5.13 pc and the determined ED , the lower limit of total R -band flare energy E_R is inferred to be $E_R = (3.3 \pm 0.2) \times 10^{32} \text{ ergs}$.

Table 3. The parameters of the four-components model resulted from our light curve fitting. k_i and a_i are the decay slope and normalization of each component, respectively.

Parameters	Value
a_1	0.508869 ± 0.007355
k_1	0.011504 ± 0.000241
a_2	0.310620 ± 0.022111
k_2	0.062431 ± 0.008285
a_3	0.116739 ± 0.003715
k_3	0.003050 ± 0.000073
a_4	0.024246 ± 0.000554
k_4	0.000270 ± 0.000010

4. OFF-LINE SEARCH FOR FLARES FROM GWAC ARCHIVE IMAGES

The on-line pipeline we have developed is intend to detect large-amplitude superflares in real-time (Xin et al. 2021). In order to study the flare activities of EI Cnc in a long term, we performed an off-line search for flares of EI Cnc, which might be missed by our on-line pipeline, in the JFoV archive images obtained from 2018

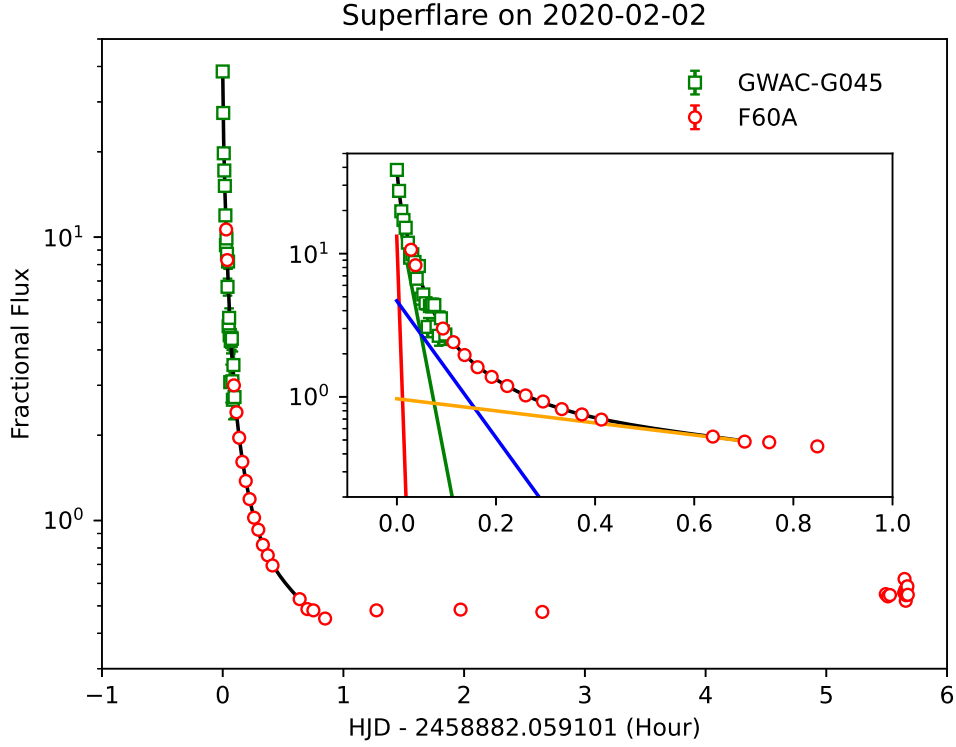


Figure 3. Combined R -band light curve of the superflare triggered by the GWAC/FFoV in 2020-02-02. The green squares refers to the data obtained by the FFoV, and the red circles the data by F60A. The black curve shows the best fit to the light curve. The four components used to reproduce the light curve are shown separately by different colors in the insert sub-panel.

October 1 to 2021 April 24. By using the data reduction methods described in Section 3.2, the long-term light curve obtained by the JFoV is shown in Figure 4. In total, the object has been recorded in 78422 images over 198 nights, spanning ~ 290 hours. Considering the fact that the flare duration is typical of tens of minutes to a few hours, our off-line search is designed as follows.

1. The light curve in each night is produced by a differential photometry with the same companion star for all the images.
2. Each generated light curve is sliced into several boxes, each with a time window of 30 minutes.
3. The medium and standard derivation (σ) are calculated in each box.
4. Any measurement with a deviation greater than $+3\sigma$ is marked.
5. A flare event candidate is flagged if there are more than three consecutively marked measurements.
6. All the candidates are examined by human eyes one by one.

As a result, in addition the superflare described in Section 3, a total of 27 flares were identified within the 2018-2021 observing seasons. The log of all the flares is shown in Table 4, in which the peak time and flare amplitude are listed in Columns (2) and (3), respectively. Figure.5 and Figure.6 display the zoom-in light curves of the 27 flares.

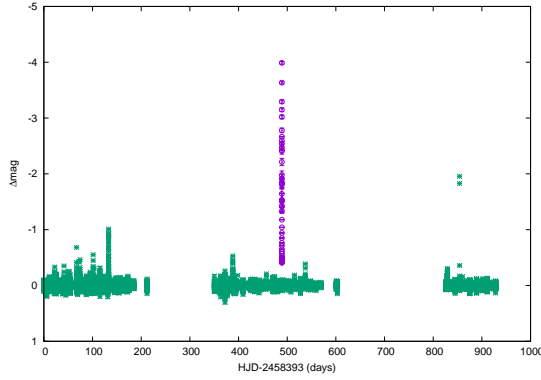


Figure 4. The long-term light curve of EI Cnc obtained by GWAC JFoV after subtracting the quiescent flux level. The super flare on 2020-02-02 is marked by the magenta circles.

One can see from the figures that five (20%) out of the 27 flares show complex eruptions with multi peaks. This fraction is higher than 12% found in the TRAPPIST-1 sample (Vida et al. 2017), simply because of the GWAC’s high cadence of 15 seconds. Based on the *K2* measurements, the cadence is ~ 59 s for the TRAPPIST-1 sample.

The energies released in these flares are estimated by the same method previously described in Section 3.3. Lower limits of the released energies are calculated for 4 out of the 27 flares without complete light curves. The measured flare amplitude and estimated E_R are tabulated in Columns (3) and (5) in Table 4, respectively. The flare amplitude ranges from $\Delta R \sim 0.1$ mag to ~ 3 mag, which corresponds to a flare energy range between $E_R = 4.0 \times 10^{29}$ erg and 3.3×10^{32} erg.

5. CUMULATIVE FLARE ENERGY DISTRIBUTION

Based on the flares reported above, we investigate the cumulative flare frequency distribution (FFD) of EI Cnc in this section. After excluding the flares with only a lower limit of E_R , the calculated FFD is plotted as a function of bolometric flaring energy E_{bol} in Figure 7. E_{bol} is converted from E_R by a bolometric

metric correction of $E_{\text{bol}} = E_R \times 6.0$ assuming 10,000K blackbody radiation (e.g., Gizis et al. 2013; Kowalski et al. 2013; Paudel et al. 2019; Murray et al. 2022; Fleming et al. 2022). The resulted FFD shows a clear deviation from the linear fit both at low and high energies. Similar feature could also be seen in other active stars, such as GJ 1245AB (Lurie et al. 2015) and GJ 1243 (Silverberg et al. 2016). One explanation for this behavior is the incomplete detection of low and high energy flares, but the possibility of a real deviation cannot be excluded (Hawley et al. 2014; Lurie et al. 2015). More intensive observations are needed to confirm this. Following the commonly used method, we fit the FFD by a linear function of

$$\log \tilde{\nu} = \alpha + \beta \log E_{\text{bol}} \quad (2)$$

where $\tilde{\nu}$ and E_{bol} are the cumulative flare frequency per day and the bolometric flare energy in unit of ergs, respectively. α and β are the normalization and distribution index, respectively. By assuming that the uncertainty of FFD could be described by a Poisson sampling following Lurie et al. (2015), a least-square fit returns $\alpha = 15.26 \pm 0.96$ and $\beta = -0.50 \pm 0.03$, along with a reduced χ^2 of 0.14 at a degree of freedom of 20. The best-fit relationship is overplotted in Figure.7 by a black line.

The distribution index β is traditionally used to characterise the flare energy distributions. For stars with $\beta > -1$, high-energy flares dominate the total energy output released in the flaring process (Paudel et al. 2018; Jackman et al. 2021). However, the total energy output is dominated by low-energy flares for the stars with $\beta < -1$, which could be understood by the heating of the quiescent corona (Parker 1988; Hudson 1991; Schrijver et al. 2012). Based on the GWAC observations, the modeled $\beta \sim -0.5$ suggests a quite shallow FFD for EI Cnc, a M7 type dwarf. This shallow FFD reinforces the trend reported recently in a comprehen-

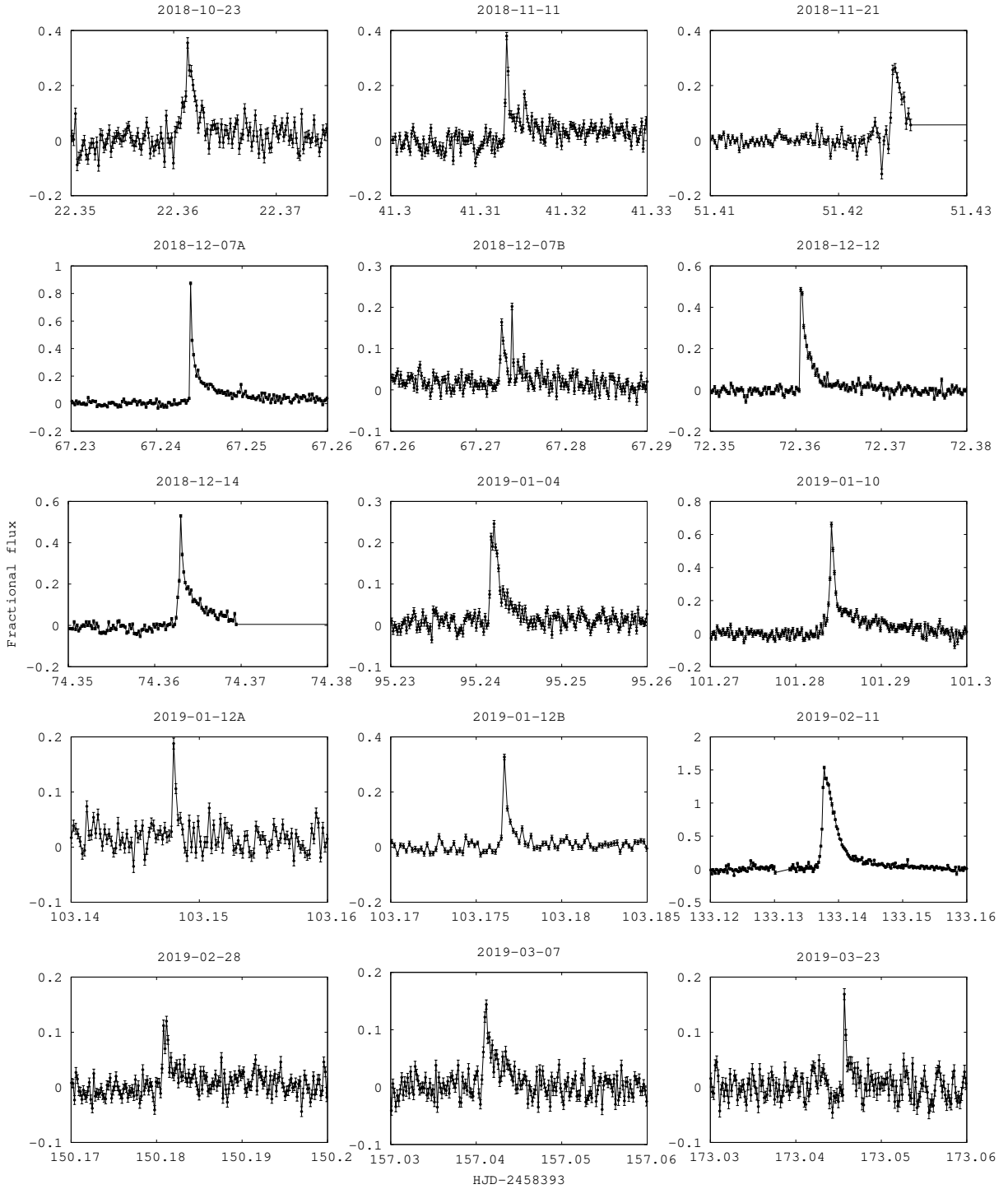


Figure 5. The R -band light curves of the 27 flares found by our off-line search in the GWAC JFoV achieved data obtained from 2018 October 1 to 2021 April 24. In order to display the main flare phase better, the tails of some of the flares are not shown due to a cutoff on the abscissa axis.

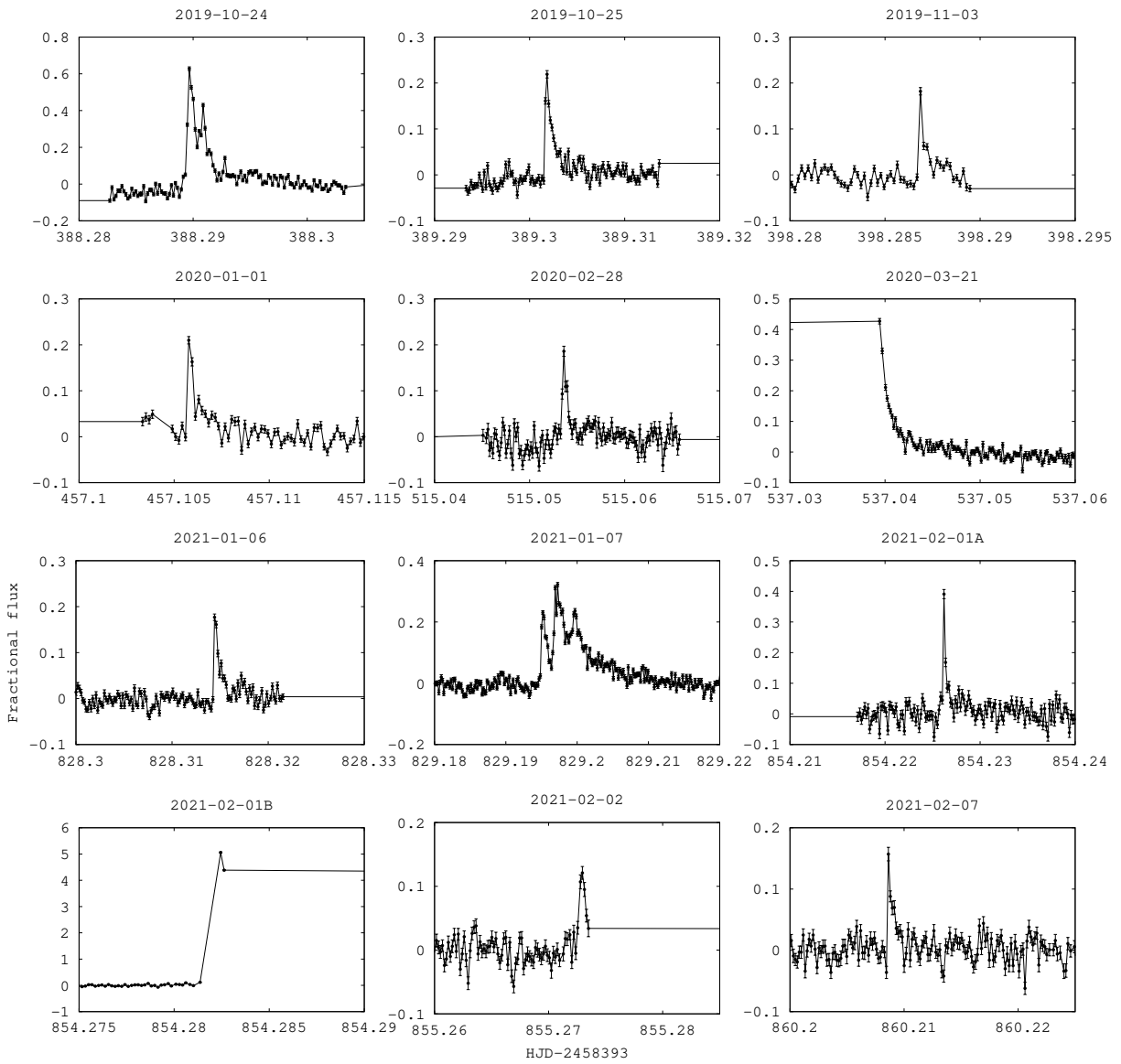


Figure 6. Continued for the Figure.5

Table 4. Properties of all the 28 flares of EI Cnc detected in this study.

No.	Peak time	ΔR	τ	E_R	B
	UT	mag	second	erg	Gauss
(1)	(2)	(3)	(4)	(5)	(6)
1	2018-10-23T20:41:53	0.34 ± 0.02	76	8.6×10^{30}	161
2	2018-11-11T19:30:20	0.36 ± 0.01	30	1.0×10^{31}	174
3	2018-11-21T22:08:32	0.25 ± 0.02	82	$> 4.6 \times 10^{30}$	> 118
4	2018-12-07T17:46:40	0.68 ± 0.01	33	2.2×10^{31}	258
5	2018-12-07T18:30:10	0.20 ± 0.01	43	4.1×10^{30}	111
6	2018-12-12T20:33:58	0.44 ± 0.01	81	9.7×10^{30}	171
7	2018-12-14T20:37:16	0.48 ± 0.01	59	1.4×10^{31}	206
8	2019-01-04T17:41:17	0.24 ± 0.01	77	6.0×10^{30}	135
9	2019-01-10T18:41:31	0.55 ± 0.01	50	1.2×10^{31}	191
10	2019-01-12T15:25:20	0.15 ± 0.01	17	4.0×10^{29}	35
11	2019-01-12T16:06:35	0.27 ± 0.01	17	6.6×10^{29}	45
12	2019-02-11T15:10:14	1.03 ± 0.01	187	6.8×10^{31}	454
13	2019-02-28T16:13:32	0.12 ± 0.01	50	1.2×10^{30}	60
14	2019-03-07T12:52:28	0.15 ± 0.01	73	2.9×10^{30}	94
15	2019-03-23T13:00:28	0.17 ± 0.01	21	1.8×10^{30}	74
16	2019-10-24T18:58:32	0.58 ± 0.01	118	3.2×10^{31}	311
17	2019-10-25T19:15:55	0.22 ± 0.01	61	5.0×10^{30}	123
18	2019-11-03T18:53:04	0.18 ± 0.01	15	6.9×10^{29}	46
19	2020-01-01T14:25:13	0.20 ± 0.01	24	1.6×10^{30}	70
20	2020-02-02T13:16:50	3.70 ± 0.01	73	3.3×10^{32}	1000
21	2020-02-28T13:09:49	0.20 ± 0.01	38	3.3×10^{30}	100
22	2020-03-21T12:51:21	$> 0.40 \pm 0.01$	86	$> 7.4 \times 10^{30}$	> 150
23	2021-01-06T19:25:31	0.18 ± 0.01	55	1.8×10^{30}	74
24	2021-01-07T16:36:01	0.32 ± 0.01	334	1.9×10^{31}	240
25	2021-02-01T17:17:27	0.36 ± 0.01	19	2.4×10^{30}	85
26	2021-02-01T18:37:23	$> 2.29 \pm 0.01$	182	$> 2.1 \times 10^{32}$	> 798
27	2021-02-02T18:24:48	0.12 ± 0.01	38	$> 1.2 \times 10^{30}$	> 60
28	2021-02-07T16:52:13	0.15 ± 0.01	52	9.8×10^{30}	172

sive study on the Kepler and TESS photometric data by Gao et al. (2022), in which, compared to early M-dwarfs, stars cooler than M4 show marginally enhanced superflare activity.

Similar to those found in a lot of previous studies (e.g. Lurie et al. 2015; Silverberg et al. 2016; Vida et al. 2017; Paudel et al. 2018; Lin et al. 2022), a close inspection of the resulted FFD shows an obvious deviation from a

single powerlaw by a "smooth" break at $E_{\text{bol}} \sim 10^{32}$ erg. Although an incompleteness of flares can not be entirely excluded, further study is needed to confirm the phenomenon and to understand the potential underlying physics.

6. DISCUSSION

6.1. A comparison study on FFD

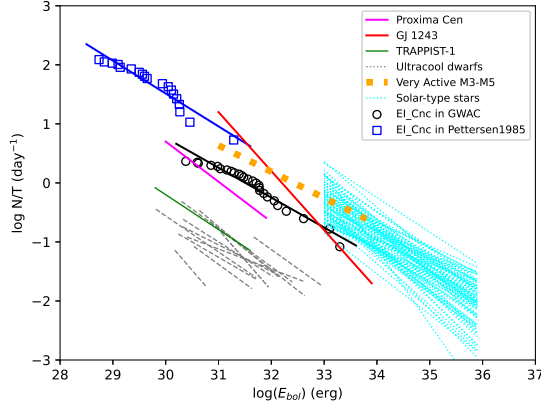


Figure 7. A comparison of the cumulative FFD. The FFDs inferred from this study and reported in Pettersen (1985) are presented by the black-open circles and by the blue-open squares, respectively. The black and blue solid lines denote the best fit linear relationships according to Eq. (2). The magenta, red and green solid lines represent of the approximate positions of FFDs of Proxima Cen, GJ 1243 and TRAPPIST-1 (Vida et al. 2017) respectively. The grey dashed lines and orange dotted line represent FFDs of ultracool dwarfs from Paudel et al. (2018) and very active M3-M5 dwarfs (Hawley et al. 2014) respectively. The cyan dotted lines refer to FFDs of solar-type stars (Gao et al. 2022).

The blue-open squares, along with the blue solid line, show the FFD of EI Cnc generated from Pettersen (1985) who reported 13 flares during 4.5 hours in the U -band. In order to compare the FFDs in different epochs, the U -band flaring energy E_U is in advance converted to E_{bol} by adopting a bolometric correction of $E_{\text{bol}} = E_U \times 6.0$, after assuming a blackbody with a temperature of 10,000K at the peak time (Kowalski et al. 2013).

Comparing this FFD measured about four decades ago with the one given in this study enables us to reveal a long term variation of the flare rate and magnetic activity of EI Cnc. The extrapolation is reasonable after taking into account of the studies of the flare activity in a number of the solar-type and cooler active

stars (e.g., Maehara et al. (2012); Paudel et al. (2018); Gao et al. (2022)), in which a global FFD slope is available for most of the stars in a wide flare energy ranging from the nano-flares ($\sim 10^{24}$ erg) to the superflares ($\sim 10^{36}$ erg).

On the other hand, at energy of $\sim 10^{31}$ erg, the FFD from Pettersen (1985) yields a flare rate of about ten times per day, which is quite close to those of active M6 dwarf Wolf 359 (Lin et al. 2022) and very active M3-M5 dwarfs (the orange dots in Figure 7) as reported by Hawley et al. (2014).

Figure 7 additionally compares the FFD of EI Cnc measured in the current study with those of other M dwarfs after adopting a relationship of $E_{\text{bol}} = 3.1E_{\text{Kp}}$ (Paudel et al. 2018), where E_{Kp} is the *Kepler* flare energy. The comparison shows that EI Cnc is in fact more active than not only the M5.5 dwarf Proxima Cen (Davenport et al. (2016), the magenta line), but also the ultracool dwarfs (the grey dashed lines) studied in Paudel et al. (2018).

Especially, the flare rate of EI Cnc is found to be at least ten times higher than that of the M8 dwarf TRAPPIST-1 (the green line, Vida et al. (2017)). Further more, compared to EI Cnc, a much steeper FFD is found for the active M4 dwarf GJ 1243. If the flaring rate of EI Cnc is extrapolated to the energy larger than 10^{34} erg from the fit of FFD, then its superflare rate with energies $E > 10^{34}$ erg would be at least one order of magnitude higher than that of GJ 1243. The reason for high superflare rate is still under debate at the current stage. There are some evidences supporting that superflares are more likely to occur on young stars with fast rotation (Howard et al. 2020). However, other studies found an enhanced superflare rate in stars with intermediate rotation periods (10-70d)(Mondrik et al. 2019).

The FFDs of solar-types stars (Gao et al. 2022) are collected and displayed in the Figure 7 as cyan dotted lines. The data from solar-

type stars have a wide distribution indicating a different level of activity. The slopes of these FFDs are similar with each other, and also comparable to the slopes of EI Cnc we derived, suggesting similar flare generation mechanism for stars from M-types to solar types.

There has been a few attempts made to explore long-term variations of cool dwarfs (eg., Buccino et al. (2011); Gomes da Silva et al. (2012); Ibañez Bustos et al. (2020); Mignon et al. (2023)). In the aspect of flaring rate, Davenport et al. (2020) reported no sign of solar-like activity cycles for the active flaring M4 dwarf GJ 1243 over 10 years. Lately, Crowley et al. (2022) found a low number of stars with detectable rate variation by analysing TESS data of 274 G type stars. For the case of EI Cnc, although the two FFDs have small common energy range, the current FFD is 5~6 times lower than the extrapolation of the FFD generated from Pettersen (1985), which may be related to the active cycles in ultra cool dwarfs, similar to those occurred on the Sun (Usoskin 2023) and solar type stars (Baliunas et al. 1995; Berdyugina 2005; Olsper et al. 2018; Boro Saikia et al. 2018; Baum et al. 2022).

6.2. The flare duration verses energy

Maehara et al. (2015) reports a correlation between white light (WL) flare energy and duration τ for the superflares of solar-like stars: $\tau \propto E^{0.39 \pm 0.03}$, where τ is defined as the e -folding decay time of flare intensity after its peak and E is defined as the bolometric energy of flares.

On the observational ground, this correlation is quite similar with not only the relationship of $\tau \propto E^{0.2-0.3}$ in the solar hard/soft X-ray flares (e.g., Veronig et al. (2002), Christe et al. (2008)), but also the relationship of $\tau \propto E^{0.39}$ revealed in the solar WL flares (Namekata et al. 2017). In addition, the validation of the $\tau - E$ relationship has been extended to mid-M dwarfs by a comprehensive study carried out by Chang et al. (2015). Such similarity therefore rein-

forces the ideal that solar and stellar flares share the same mechanism: the magnetic reconnection, although there is some difference in the relationship between the field mid-M dwarfs and the mid-M stars in open cluster (Chang et al. 2015). On the theoretical ground, a $\tau \propto E^{1/3}$ relationship could be obtained in the magnetic reconnection scenario, if both magnetic field strength B and Alfvén velocity $v_A = B/\sqrt{4\pi\rho}$ are taken to be constants (Maehara et al. 2015).

Following Maehara et al. (2015), we show the $\tau - E$ relationship for the WL flares detected in EI Cnc by the red circles in Figure.8. The measured τ of each of the flares are listed in Column (4) in Table 4. E is obtained from the measured E_R by a transform used by Maehara et al. (2015). In contrast to the results of the Sun given in Namekata et al. (2017), the figure shows that the WL flares detected in EI Cnc closely follow the $\tau - E$ relationship established in the WL superflares of the solar-type stars by extending the flare energy down to $\sim 10^{30}$ erg, which suggests that the late-M dwarfs and the partially convective solar-type stars share a common flare mechanism. Combining the two data sets shown in the figure returns a best-fit $\tau - E$ relationship

$$\tau \propto E^{0.42 \pm 0.02} \quad (3)$$

which is valid for the flares of both late-M dwarfs and solar-type stars.

Assuming τ is comparable to the reconnection timescale, the complete scaling law can be expressed as $\tau \propto E^{1/3} B^{-2/3} v_A^{-1} M_A^{-1}$ (Namekata et al. 2017), where τ and E refer to the e -folding decay time and the bolometric energy of flares respectively, v_A is the Alfvén velocity, and M_A is the dimensionless reconnection rate ranging from 0.1 to 0.01 in the Petschek-type fast reconnection (e.g., Shibata & Magara 2011). Taking into account of the considerable difference in B and ρ between late-M dwarfs and solar-type stars, the universal $\tau - E$ rela-

relationship shown in the figure implies $B^{2/3}v_A$ is an invariant in the (super)WL flares on stars with different types.

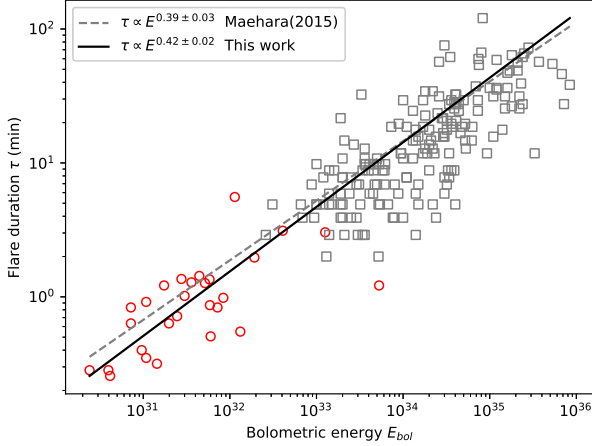


Figure 8. The flare duration e -folding time τ versus the bolometric flare energy. The red circles and black squares denote the flares detected in M7 dwarf EI Cnc in this work and the superflares on G-type stars detected from the Kepler short cadence data by Maehara et al. (2015), respectively. The dashed line shows the best fit $\tau - E$ relationship given in Maehara et al. (2015), when the superflares are considered. After including the flares in EI Cnc, an updated $\tau - E$ relationship is overplotted by the solid line.

6.3. Estimation of magnetic field

Based on the solar flare model, the magnetic field strength B of EI Cnc can be estimated from flare energy E_{flare} according to (Shibata et al. 2013):

$$E_{\text{flare}} \approx 7 \times 10^{32} (\text{erg}) \left(\frac{f}{0.1} \right) \left(\frac{B}{10^3 \text{G}} \right)^2 \left(\frac{A_{\text{spot}}}{3 \times 10^{19} \text{cm}^2} \right)^{3/2} \quad (4)$$

where f is the fraction of magnetic energy that can be released as flare energy. $A_{\text{spot}} = 4\pi R_*^2 f_{\text{spot}}$ is the area of spot on a star, where R_* is the stellar radius and $f_{\text{spot}} < 1$ the fraction of stellar area.

The value of B of each of the flares identified in this study is estimated by adopting a typical value of $f = 0.1$ (Aschwanden et al. 2014; Jackman et al. 2018) and the estimated stellar radius of $R_* \sim 0.2R_{\odot}$ for EI Cnc (Gershberg et al. 1999), and listed in column (6) in Table 4. A fiducial value of $f_{\text{spot}} = 0.1$ is used in the estimations. The estimated B has a value of $\sim 10^3 \text{Gauss}$ for the energetic flares with $E \sim 10^{33} \text{erg}$, which is comparable to those estimated for other superflares of later M dwarfs (e.g., Paudel et al. 2018; Xin et al. 2021).

7. SUMMARY

An optical monitoring campaign on the nearby flaring system EI Cnc was carried out by the GWAC and its dedicated follow-up telescope, which allows us to arrived at following results.

1. A superflare with a lower limit of R band flare energy $\sim 3.3 \times 10^{32} \text{erg}$ was triggered and observed, in which four components are required to properly model the complex decay light curve. Rapid follow-ups revealed that the flare was generated by the brighter component of the binary EI CncA.
2. Combining the 27 flares additionally detected from the GWAC achieve data leads to a quite shallow FFD with $\beta = -0.50 \pm 0.03$ over an energy range between 10^{30}erg and 10^{33}erg , which supports an dominance of high-energy flares in the the flare activity in EI Cnc.
3. The significant decreasing flare rate is obtained compared with the observations about four decades ago, which is probably related to the active cycles in ultra cool dwarfs.
4. The white-light (super)flares from late M dwarf and solar-type stars are found to follow an updated $\tau - E$ relationship $\tau \propto$

$E^{0.42 \pm 0.02}$, which implies a universal mechanism in the stellar flare activity.

8. ACKNOWLEDGEMENT

We thank the anonymous referee for helpful comments that allow us to improve the paper significantly. This study is supported from the National Natural Science Foundation of China (Grant No. 11973055, U1938201, U1831207, U1931133,12133003) and partially supported by the Strategic Pioneer Program on Space Science, Chinese Academy of Sciences, grant Nos. XDA15052600 and XDA15016500. JW is supported by the National Natural Science Foundation of China under grants 12173009 and by the Natural Science. Foundation of Guangxi (2020GXNSFDA238018). DWX is supported by the National Natural Science Foundation of China under grant 12273054. YGY is supported by the National Natural Science Foun-

dation of China under grant 11873003. HBC is supported by the National Natural Science Foundation of China under grant 11973063. This research has made use of the VizieR catalogue access tool, CDS, Strasbourg, France (DOI: 10.26093/cds/vizier). The original description of the VizieR service was published in A&AS 143, 23. This work has made use of data from the European Space Agency (ESA) mission *Gaia* (<https://www.cosmos.esa.int/gaia>), processed by the *Gaia* Data Processing and Analysis Consortium (DPAC, <https://www.cosmos.esa.int/web/gaia/dpac/consortium>) Funding for the DPAC has been provided by national institutions, in particular the institutions participating in the *Gaia* Multilateral Agreement.

Facilities: GWAC, GWAC-F60 telescope

Software: IRAF (Tody 1986, 1992)

REFERENCES

- Aschwanden, M. J., Xu, Y., & Jing, J., 2014,ApJ,797,50
- Baliunas, S. L., Donahue, R. A., Soon, W. H., et al., 1995,ApJ,438,269
- Barnes, S. A., 2003,ApJ,586,464
- Baum, A. C., Wright, J. T., Luhn, J. K., & Isaacson, H., 2022,AJ,163,183
- Berdyugina, S. V., 2005,LRSP,2,8
- Bochanski, J. J., Hawley, S. L., Covey, K. R., et al., 2010,AJ,139,2679
- Boro Saikia, S., Marvin, C. J., Jeffers, S. V., et al., 2018,A&A,616,A108
- Buccino, A. P., Díaz, R. F., Luoni, M. L., Abrevaya, X. C., & Mauas, P. J. D., 2011,AJ,141,34
- Ibañez Bustos, R. V., Buccino, A. P., Messina, S., Lanza, A. F., & Mauas, P. J. D., 2020,A&A,644,A2
- Chabrier, G., & Baraffe, I., 1997,A&A,327,1039
- Chang, S.-W., Byun, Y.-I., & Hartman, J. D., 2015,ApJ,814,35
- Charbonneau, P., 2014,ARA&A,52,251
- Christe, S., Hannah, I. G., Krucker, S., McTiernan, J., & Lin, R. P., 2008,ApJ,677,1385
- Crowley, J., Wheatland, M. S., & Yang, K., 2022,ApJ,941,193
- Davenport, J. R. A., Mendoza, G. T., & Hawley, S. L., 2020,AJ,160,36
- Davenport, J. R. A., Kipping, D. M., Sasselov, D., Matthews, J. M., & Cameron, C., 2016,ApJL,829,L31
- De Luca, A., Stelzer, B., Burgasser, A. J., et al., 2020,A&A,634,L13
- Fleming, T. A., Schmitt, J. H. M. M., & Giampapa, M. S., 1995,ApJ,450,401
- Fleming, T. A., Giampapa, M. S., & Schmitt, J. H. M. M., 2000,ApJ,533,372
- Fleming, S. W., Million, C., Osten, R. A., Kolotkov, D. Y., & Brasseur, C. E., 2022,ApJ,928,8
- Fuhrmeister, B., & Schmitt, J. H. M. M., 2004,A&A,420,1079
- Fuhrmeister, B., Schmitt, J. H. M. M., & Wichmann, R., 2004,A&A,417,701

- Gaia Collaboration, Brown, A. G. A., Vallenari, A., et al., 2018,*A&A*,616,A1
- Gaia Collaboration, Brown, A. G. A., Vallenari, A., et al., 2021,*A&A*,649,A1
- Gao, D.-Y., Liu, H.-G., Yang, M., & Zhou, J.-L., 2022,*AJ*,164,213
- Gershberg, R. E., Katsova, M. M., Lovkaya, M. N., Terebizh, A. V., & Shakhovskaya, N. I., 1999,*A&AS*,139,555
- Gizis, J. E., Burgasser, A. J., Berger, E., et al., 2013,*ApJ*,779,172
- Gizis, J. E., Paudel, R. R., Mullan, D., et al., 2017,*ApJ*,845,33
- Gizis, J. E., Monet, D. G., Reid, I. N., et al., 2000,*AJ*,120,1085
- Han, X., Xiao, Y., Zhang, P., et al., 2021,*PASP*,133,065001
- Hawley, S. L., Davenport, J. R. A., Kowalski, A. F., et al., 2014,*ApJ*,797,121
- Henry, T. J., Jao, W.-C., Subasavage, J. P., et al., 2006,*AJ*,132,2360
- Howard, W. S., Corbett, H., Law, N. M., et al., 2020,*ApJ*,895,140
- Hudson, H. S., 1991,*SoPh*,133,357
- Jackman, J. A. G., Wheatley, P. J., Pugh, C. E., et al., 2018,*MNRAS*,477,4655
- Jackman, J. A. G., Shkolnik, E., & Loyd, R. O. P., 2021,*MNRAS*,502,2033
- Kanodia, S., Ramsey, L. W., Maney, M., et al., 2022,*ApJ*,925,155
- Khodachenko, M. L., Ribas, I., Lammer, H., et al., 2007,*AsBio*,7,167
- Kochukhov, O., 2021,*A&ARv*,29,1
- Kowalski, A. F., Hawley, S. L., Wisniewski, J. P., et al., 2013,*ApJS*,207,15
- Lammer, H., Lichtenegger, H. I. M., Kulikov, Y. N., et al., 2007,*AsBio*,7,185
- Law, N. M., Hodgkin, S. T., & Mackay, C. D., 2008,*MNRAS*,384,150
- Li, G.-W., Wu, C., Zhou, G.-P., et al., 2023,*RAA*,23,015016
- Lin, H.-T., Chen, W.-P., Liu, J., et al., 2022,*AJ*,163,164
- Lurie, J. C., Davenport, J. R. A., Hawley, S. L., et al., 2015,*ApJ*,800,95
- Maehara, H., Shibayama, T., Notsu, Y., et al., 2015,*EP&S*,67,59
- Maehara, H., Shibayama, T., Notsu, S., et al., 2012,*Natur*,485,478
- McLean, M., Berger, E., & Reiners, A., 2012,*ApJ*,746,23
- Medina, A. A., Winters, J. G., Irwin, J. M., & Charbonneau, D., 2020,*ApJ*,905,107
- Mignon, L., Meunier, N., Delfosse, X., et al., 2023,*arXiv*,arXiv:2303.03998
- Mohanty, S., Basri, G., Shu, F., Allard, F., & Chabrier, G., 2002,*ApJ*,571,469
- Mondrik, N., Newton, E., Charbonneau, D., & Irwin, J., 2019,*ApJ*,870,10
- Morin, J., Donati, J.-F., Petit, P., et al., 2010,*MNRAS*,407,2269
- Monet, D. G., Levine, S. E., Canzian, B., et al., 2003,*AJ*,125,984
- Murray, C. A., Queloz, D., Gillon, M., et al., 2022,*MNRAS*,513,2615
- Namekata, K., Sakaue, T., Watanabe, K., et al., 2017,*ApJ*,851,91
- Newton, E. R., Charbonneau, D., Irwin, J., et al., 2014,*AJ*,147,20
- Olsper, N., Lehtinen, J. J., Käpylä, M. J., Pelt, J., & Grigorievskiy, A., 2018,*A&A*,619,A6
- Parker, E. N., 1988,*ApJ*,330,474
- Paudel, R. R., Gizis, J. E., Mullan, D. J., et al., 2018,*ApJ*,858,55
- Paudel, R. R., Gizis, J. E., Mullan, D. J., et al., 2019,*MNRAS*,486,1438
- Pettersen, B. R., & Evans, D. S., 1985,*BAAS*,17,437
- Pettersen, B. R., 1985,*A&A*,148,151
- Pettersen, B. R., 2006,*MNRAS*,368,1392
- Pettersen, B. R., 1991,*MmSAI*,62,217
- Ranjan, S., Wordsworth, R., & Sasselov, D. D., 2017,*ApJ*,843,110
- Reid, I. N., & Gizis, J. E., 1997,*AJ*,113,2246
- Rimmer, P. B., Xu, J., Thompson, S. J., et al., 2018,*SciA*,4,eaar3302
- Robrade, J., Poppenhaeger, K., & Schmitt, J. H. M. M., 2010,*A&A*,513,A12
- Boro Saikia, S., Marvin, C. J., Jeffers, S. V., et al., 2018,*A&A*,616,A108
- Schmidt, S. J., Shappee, B. J., Gagné, J., et al., 2016,*ApJL*,828,L22
- Schmidt, S. J., Prieto, J. L., Stanek, K. Z., et al., 2014,*ApJL*,781,L24
- Schmitt, J. H. M. M., & Liefke, C., 2004,*A&A*,417,651
- Schmitt, J. H. M. M., Fleming, T. A., & Giampapa, M. S., 1995,*ApJ*,450,392

- Schrijver, C. J., Beer, J., Baltensperger, U., et al., 2012, *JGRA*, 117, A08103
- Segura, A., Walkowicz, L. M., Meadows, V., Kasting, J., & Hawley, S., 2010, *AsBio*, 10, 751
- Shibata, K., Isobe, H., Hillier, A., et al., 2013, *PASJ*, 65, 49
- Shibata, K., & Magara, T., 2011, *LRSP*, 8, 6
- Shields, A. L., Ballard, S., & Johnson, J. A., 2016, *PhR*, 663, 1
- Gomes da Silva, J., Santos, N. C., Bonfils, X., et al., 2012, *A&A*, 541, A9
- Silverberg, S. M., Kowalski, A. F., Davenport, J. R. A., et al., 2016, *ApJ*, 829, 129
- Stelzer, B., Schmitt, J. H. M. M., Micela, G., & Liefke, C., 2006, *A&A*, 460, L35
- Tilley, M. A., Segura, A., Meadows, V., Hawley, S., & Davenport, J., 2019, *AsBio*, 19, 64
- Turpin, D., Wu, C., Han, X.-H., et al., 2020, *RAA*, 20, 013
- Usoskin, I. G., 2023, *LRSP*, 20, 2
- Veronig, A., Temmer, M., Hanslmeier, A., Otruba, W., & Messerotti, M., 2002, *A&A*, 382, 1070
- Vida, K., Kővári, Z., Pál, A., Oláh, K., & Kriskovics, L., 2017, *ApJ*, 841, 124
- Wang, J., Li, H. L., Xin, L. P., et al., 2020, *AJ*, 159, 35
- Wang, J., Xin, L. P., Li, H. L., et al., 2021, *ApJ*, 916, 92
- Wang, Y.-F., Luo, A.-L., Chen, W.-P., et al., 2022, *A&A*, 660, A38
- Wang, Y.-F., Luo, A.-L., Chen, W.-P., et al., 2022, *A&A*, 660, A38
- Wei, J., Cordier, B., Antier, S., et al., 2016, *arXiv*, arXiv:1610.06892
- Xin, L. P., Li, H. L., Wang, J., et al., 2021, *ApJ*, 922, 78
- Xin, L. P., Li, H. L., Wang, J., et al., 2021, *ApJ*, 909, 106
- Xin, L.-P., Li, H.-. li ., Wang, J., et al., 2023, *MNRAS*.tmp
- Xin, L., Han, X., Li, H., et al., 2023, *NatAs*.tmp
- Xu, Y., Xin, L. P., Wang, J., et al., 2020, *PASP*, 132, 054502
- Zeldes, J., Hinkle, J. T., Shappee, B. J., et al., 2021, *arXiv*, arXiv:2109.04501